Journal of Materials Chemistry C

Ferroelectric 2D Antimony Oxides with Wide Bandgaps

Journal:	*Journal of Materials Chemistry C*
Manuscript ID	TC-ART-08-2022-003343.R1
Article Type:	Paper
Date Submitted by the Author:	01-Nov-2022
Complete List of Authors:	Bhattarai, Romakanta; The University of Memphis, Physics and Materials Science Ni, Kai; Rochester Institute of Technology, Shen, Xiao; University of Memphis, Physics and Materials Science

ARTICLE

Ferroelectric 2D Antimony Oxides with Wide Bandgaps

Romakanta Bhattarai[a], Kai Ni[b], and Xiao Shen[a,*]

Received 00th January 20xx,
Accepted 00th January 20xx

DOI: 10.1039/x0xx00000x

The first two-dimensional (2D) polymorphs of antimony dioxide, namely, γ-Sb_2O_4 and δ-Sb_2O_4, are predicted using the evolutionary algorithm combined with first-principles density functional theory (DFT) calculations. Out-of-plane ferroelectricity is found in γ-Sb_2O_4, while in-plane ferroelectricity is found in δ-Sb_2O_4. The predicted dipole moments of γ-Sb_2O_4 and δ-Sb_2O_4 phases are 36.63 and 14.96 eÅ, respectively, implying that they can be good candidates for making ferroelectric devices. The calculations show that doping with other group V elements or applying strain can lower the switching energy barriers and thus facilitate switching. Results from GW calculations show indirect band gaps of 5.51 and 3.39 eV for γ-Sb_2O_4 and δ-Sb_2O_4 in their monolayers, respectively. Raman spectra are calculated to facilitate the experimental investigation of the predicted structures. The existence of both in-plane and out-of-plane 2D ferroelectricity and the large band gaps make this material system particularly interesting for potential applications.

Introduction

Ferroelectricity arises from a switchable spontaneous electric polarization in materials and is an intriguing feature in a wide range of materials. Ferroelectric materials have many potential applications, such as nonvolatile memory devices including ferroelectric capacitors and ferroelectric field effect transistor, and sensors.[1,2] One major challenge in using these materials in miniature devices is the depolarization field developed as the material's thickness decreases, which often destroys the ferroelectricity by inhibiting the electric polarization.[3,4] The two-dimensional (2D) van der Waals materials, however, offer an alternative path to overcome this problem, as recent findings of ferroelectric 2D materials make it possible to shrink the thicknesses of the ferroelectric devices down to atomic layers.[5–9] The robustness of ferroelectricity in 2D materials against the depolarization field mainly originates from the polarization-locking mechanism enforced by the asymmetric configuration of covalent bonds,[10] which is different from ferroelectricity in conventional ferroelectrics stabilized by long-range Coulomb interaction. 2D ferroelectrics include CuCl,[11] MX (M=Sn,Ge;X=S,Se),[12] SnTe,[7] In_2Se_3,[6,13] As_2X_3 (X=S, Se, Te),[6,14] WTe_2,[9] $CuInP_2S_6$,[8] some of which are also

[a] Department of Physics and Materials Science, The University of Memphis, Memphis, TN, USA, xshen1@memphis.edu
[b] Department of Electrical and Microelectronic Engineering, Rochester Institute of Technology, Rochester, NY, USA
* xshen1@memphis.edu

Electronic Supplementary Information (ESI) available: [details of any supplementary information available should be included here]. See DOI: 10.1039/x0xx00000x

realized in the experiment.[6–9,13,15,16] However, most of them show the in-plane electric polarization, which limits their applications in practical devices. The out-of-plane ferroelectricity, typically more desirable for nonvolatile memory applications, is extremely rare in 2D materials.[8,9,13] More importantly, a large bandgap is desirable for applications as it enables a large voltage being applied and low leakage current, but most 2D ferroelectrics known so far have small bandgaps. Under these circumstances, the Sb-O system is particularly interesting because of its rich structures, possibility to possess large band gaps, and interesting dielectric properties.[17–19]

Several phases of antimony oxides have been investigated experimentally or theoretically. Among them, the α and β phases of Sb_2O_3 and Sb_2O_4 are the most studied. They are semiconductors with direct and indirect band gaps and smaller effective masses of the carriers.[20–24] These compounds have several applications ranging from catalysis to polymerization to coating.[25–30] Zhang et al. investigated a number of layered antimonene oxides theoretically and found their band gaps ranging from 0 to 2.28 eV, along with 18Sb-18O as a topological insulator.[31] Theoretical investigation on other 2D Sb_2O_x (x= 1, 2, 3) was reported by Wolff et al.[17] Recently, Yang et al. reported experimental observation of new antimony oxide, $SbO_{1.93}$, in ultrathin samples, with an unusually large band gap (~ 6.3 eV) and a large static dielectric constant (~100).[19] Interestingly, antimony supphoiodide (SbSI) has long been known as a quasi-one-dimensional ferroelectric semiconductor,[32,33] which suggests the potential of ferroelectricity in low-dimensional Sb compounds.

In this paper, we propose two new layered phases of the antimony oxide, named γ-Sb_2O_4, and δ-Sb_2O_4, from the evolutionary algorithm combined with the first-principles calculations. Out-of-plane ferroelectricity is predicted in γ-Sb_2O_4, while in-plane ferroelectricity is predicted in δ-Sb_2O_4. We also show that the doping and strain can be used to adjust the switching energy barrier. The large dipole moment of γ-Sb_2O_4 and δ-Sb_2O_4 imply that they can be good candidates for ferroelectric applications. Their monolayers feature large band gaps. The Raman properties are also predicted. The results highlight the rich structures and properties of the Sb-O system. The finding of out-of-plane and in-plane 2D ferroelectric oxides with large bandgaps are important for potential applications of the 2D ferroelectrics.

Results

We used a genetic algorithm in combination with the density functional theory (DFT) to search for the stable structures corresponding to the local energy minimum. Details of the computational methods can be found in Supplementary Information, Section I. A total of 13130 structures are generated from the genetic algorithm with varying unit sizes, stoichiometry, and dimensionality. Among them, we obtain a total of three stable phases of Sb_2O_4. One of them is the known α-Sb_2O_4, whose appearance validates our methodology. The other two phases of Sb_2O_4 have not been reported previously, and we name them γ- and δ-Sb_2O_4. It is interesting that these new phases, which are the first 2D antimony oxides with the stoichiometric ratio of 2:4, are found by the genetic algorithm in both the 3D and 2D searches. Figure 1 shows the crystal structures of the predicted phases. For δ-Sb_2O_4, we explored the ABAB and ABBA types of stackings and found that the energy of ABAB stacking is lowered by 0.02 eV/atom. Therefore, we only focus on ABAB type of stackings, as shown in Fig. 1(c, d).

The optimized lattice parameters of the predicted structures are shown in Table 1. Both γ- and δ-Sb_2O_4 monolayers have rectangular symmetry, while their bulk crystal structures have lower symmetry due to the sliding in the stacking of the layers. The dynamical and thermal stabilities of the predicted structures are confirmed by the interlayer coupling energies, phonon spectra, and molecular dynamics simulations, as shown in Supplementary Information, Section II. The calculated exfoliation energies are 0.39 J/m^2 and 0.68 J/m^2 for γ- and δ-Sb_2O_4, respectively, which are comparable to the reported experimental exfoliation energies of graphene (0.39 J/m^2)[34] and MoS_2 (0.60 J/m^2).[35] This indicates that the experimental fabrication of γ-Sb_2O_4 and δ-Sb_2O_4 is feasible. In addition, the chemical stabilities of both phases in the ambient environments are confirmed by investigating their interactions with CO_2 and H_2O, similar to those done in In_2Se_3.[36] (See Supplementary Information, Section II.)

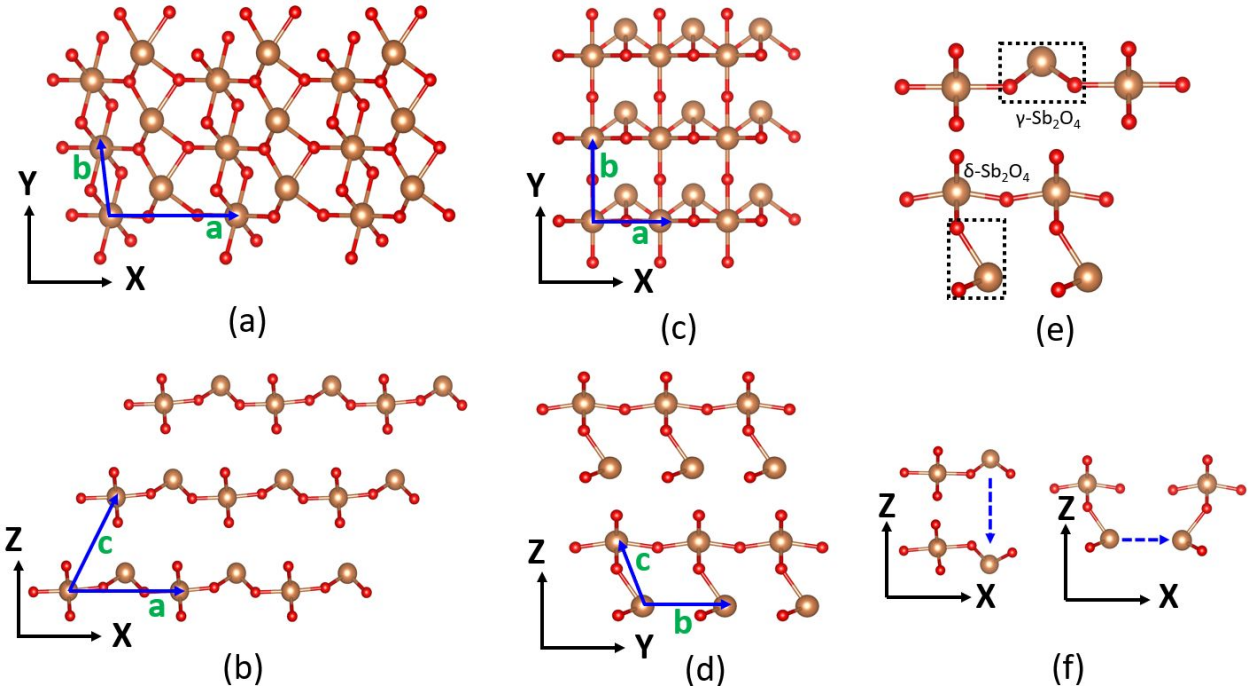

Figure 1: Crystal structures of γ-Sb_2O_4 in the top view (a) and side view (b). The top and side views for δ-Sb_2O_4 are presented in (c) and (d), respectively. (e) Schematic of γ-Sb_2O_4 and δ-Sb_2O_4 highlighting the locations of non-octahedral Sb-O bonds. (f) Ferroelectric switching in tetrahedrally bonded Sb-O dipole in γ-Sb_2O_4 and δ-Sb_2O_4 phases. Sb and O atoms are shown in brown and red colors, respectively. The lattice vectors 'a', 'b', and 'c' are represented by solid blue lines with the green labels.

First, we examine the bonding configurations in these Sb_2O_4 phases. In γ-Sb_2O_4, two types of covalent bonding between antimony and oxygen atoms are observed, as clearly shown in Fig. 1(a). Type one consists of an Sb atom bonded octahedrally (6-fold) with six neighboring oxygen atoms, whereas in type two, each Sb atom is tetrahedrally (4-fold) bonded to four oxygen atoms. Four among the six oxygen atoms around the octahedrally bonded Sb are two-fold coordinated, connecting only with the octahedral Sb atoms. On the other hand, all the four oxygens around the tetrahedrally bonded Sb are three-fold coordinated, with two bonds connecting to

tetrahedrally bonded Sb atoms and the third bond tetrahedrally bonded Sb atoms and the third bond connecting to octahedrally bonded Sb atoms. In δ-Sb_2O_4, a slight modification in bonding between Sb and O is observed. As shown in Fig. 1(b), one type of Sb is octahedrally (6-fold) bonded with six oxygen atoms as in the previous case, whereas the other Sb atom is bonded to only three oxygen atoms (3-fold). The oxygen atoms have two-fold and three-fold covalent bonds with Sb, similar to the case of γ-Sb_2O_4. Interestingly, in δ-Sb_2O_4, the two types of Sb-O bonds are in two different planes within a single layer, while in γ-Sb_2O_4, the two bonding types appear alternatingly along one direction within the same plane (Figure 1(e)). A detailed analysis of bonding environments among the γ- and δ-Sb_2O_4 phases and their corresponding bond lengths are presented in Supplementary Information, Section III.

Table 1: Optimized lattice parameters of γ-Sb_2O_4 and δ-Sb_2O_4

Phase	a (Å)	b (Å)	c (Å)	α (°)	β (°)	γ (°)	Volume (Å^3)	Bravais Lattice
γ-Sb_2O_4 (bulk)	6.55	3.06	5.87	75.4	61.4	90.2	99.09	Triclinic
γ-Sb_2O_4(monolayer)	6.50	3.05	-	90	90	90	-	Rectangular
δ-Sb_2O_4 (bulk)	3.18	3.88	6.99	102.8	90	90	84.38	Triclinic
δ-Sb_2O_4 (monolayer)	3.16	3.88	-	90	90	90	-	Rectangular

These new layered Sb_2O_4 phases exhibit interesting ferroelectric properties, as the 4-fold and 3-fold Sb in γ- and δ-Sb_2O_4 are associated with electric dipoles switchable by an external electric field. As a result of their corresponding crystal structures, the γ-Sb_2O_4 phase exhibits an out-of-plane ferroelectric switching, and the δ-Sb_2O_4 phase exhibits an in-plane dipole switching (Fig. 1(f)). The calculated switching barriers for bulk phases of γ- and δ-Sb_2O_4 are shown in Figure 2. The maximum switching energy barrier for the dipole in γ-Sb_2O_4 is found to be 0.51 eV (Figure 2(a)), whereas, for δ-Sb_2O_4, it is 0.43 eV (Figure 2(b)). We also explore the feasibility of reducing the energy barrier through doping at the Sb site. It is found that the barrier is lowered to 0.44 eV upon doping of Bi in γ-Sb_2O_4, while it is decreased to 0.29 eV upon doping of As in δ-Sb_2O_4. The doped phases remain semiconducting, as shown in Supplementary Information, Section VI. These values are comparable to the switching barriers in AlN and 2D In_2Se_3[37,13], and smaller than $GaFeO_3$.[38] We also investigate the effect of strain in the γ-Sb_2O_4 phase by applying a tensile strain of +3% along the 'a' & 'b' axis and -3% along the 'c' axis. The energy barrier is decreased by 0.13 eV to 0.38 eV, suggesting that the strain can be another method to decrease the switching barrier in the γ-Sb_2O_4. The electric dipole moment in γ-Sb_2O_4 is 36.63 eÅ per unit cell in the out-of-plane direction, whereas in δ-Sb_2O_4, the moment is 14.96 eÅ per unit cell along the in-plane direction. These values are comparable with the croconic acid and $GaFeO_3$,[38,39] and imply that they can be good candidates for ferroelectric applications.

The structural anisotropy in the Sb_2O_4 phases enables them to possess interesting properties, including ferroelectricity which arises from the breaking of the 180° inversion symmetry in-plane (δ phase) and out-of-the plane (γ phase). Further, the variability of Sb-O bonds

arising from the lattice distortion results in the double- and single-well soft mode potentials in γ- and δ- phase, resembling some of the previously studied ferroelectrics[6,12,14]. In SbSI, a well-known Sb-based ferroelectric material investigated several decades ago, and the ferroelectric behavior is associated with thermal fluctuations, change in electronic structure, atomic disorder, and phonon interactions,[40] all closely related to the variability of bonding between Sb and S/I. The finding of 2D ferroelectric Sb_2O_4 is another manifestation of the rich behavior of Sb-based compounds and its potential for future discoveries. As we will discuss below, the Sb-O system further provides an avenue for ferroelectrics with large band gaps, which are beneficial for the applications.

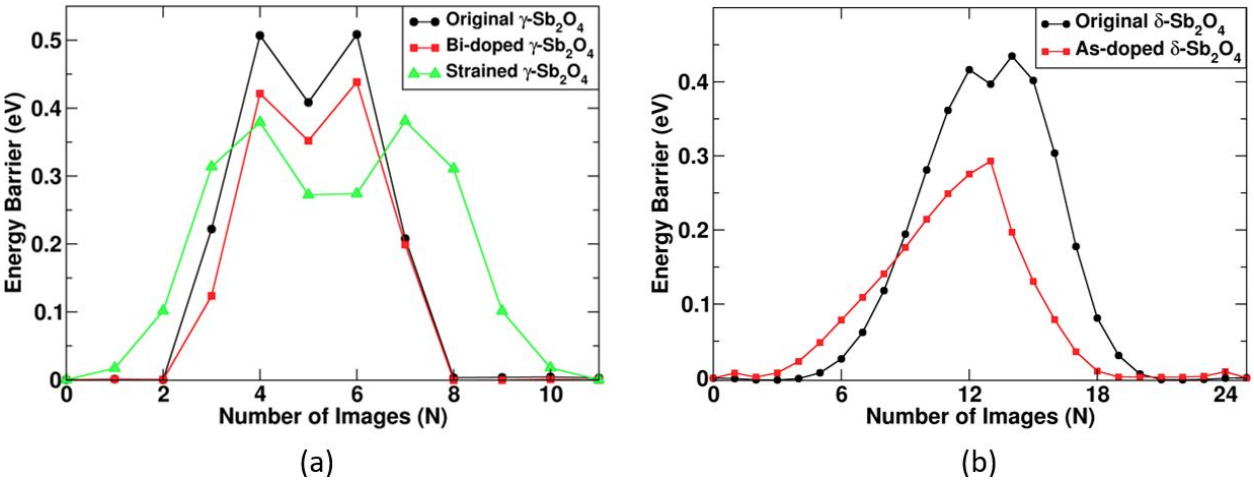

Figure 2: Switching energy barriers of (a) bulk γ-Sb_2O_4 and (b) bulk δ-Sb_2O_4 phases using the solid-state NEB method. The slight asymmetry is due to the influence of stacking.

The electronic band structures of γ-Sb_2O_4 and δ-Sb_2O_4 using the standard DFT method are shown in Figure 3. The spin-orbit effects are considered in the calculations. In the bulk γ-Sb_2O_4 (Fig. 3(a)), the maximum of the valence band (VBM) lies between the Γ and V points, whereas the minimum of the conduction band (CBM) lies at the Z point in the Brillouin zone, giving rise to an indirect band gap of 1.88 eV. In bulk δ-Sb_2O_4 (Fig. 3(b)), the VBM lies between Γ and Z (very close to Z), and CBM lies at T, giving rise to an indirect band gap of 0.63 eV. The band structures of corresponding monolayers are shown in Figs. 4(a) and 4(b). In γ-Sb_2O_4 monolayer, VBM and CBM are located between Γ & X and Γ & Y, which give rise to an indirect band gap of 2.63 eV, whereas in δ-Sb_2O_4 monolayer, they are located at G, and between S & Y, thus making an indirect band gap of 0.96 eV. We also calculated the density of states (DOS) in each configuration. The compositions of DOS are similar in all cases, and therefore only the DOS of γ-Sb_2O_4 is presented in Figure 4(c). The p-orbitals of Sb and O atoms are dominant in both the valence band and conduction band (with p-orbitals of O in higher magnitude), while contributions from the respective s-orbitals are negligible.

To get further insight into the electronic properties, we perform the Bader charge analysis in the bulk phases. In γ-Sb_2O_4, each octahedrally bonded Sb atom loses a charge of 2.66e (e being the electron charge of -1.67×10^{-19} C) to oxygen, whereas each tetrahedrally bonded Sb atom loses relatively less charge (1.83e). Each two-fold

coordinated oxygen receives a charge of 1.11e, whereas each three-fold coordinated oxygen receives a slightly more charge of 1.14e. In δ-Sb_2O_4, the corresponding values are 2.28e & 1.81e for Sb atoms, and 1.13e & 1.15e for the oxygen atoms. This charge transfer mechanism is consistent with the fact that the oxygen is more electronegative than the antimony atom.

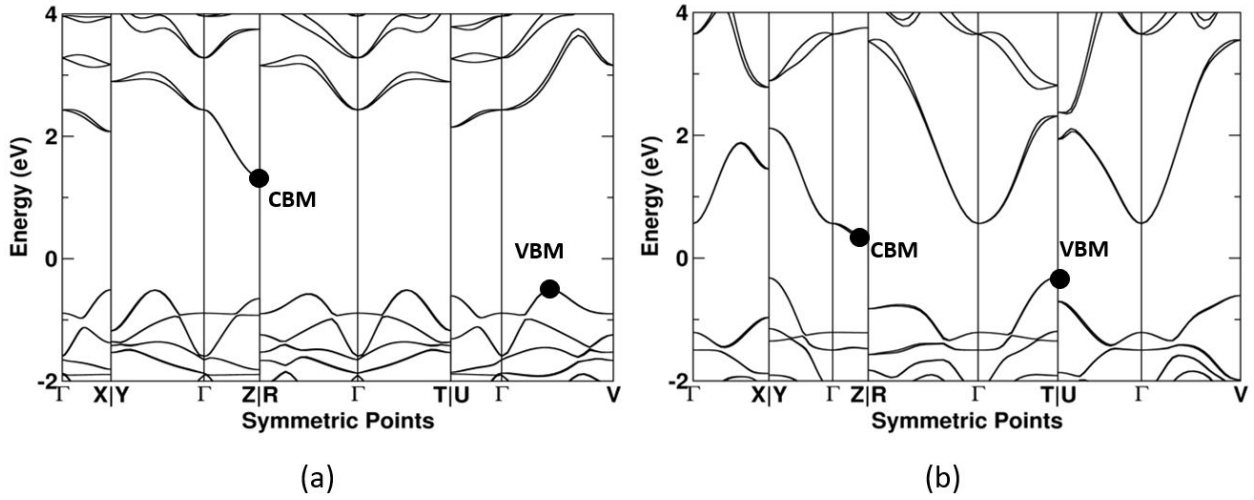

Figure 3: Band structures of (a) bulk γ-Sb_2O_4, and (b) bulk δ-Sb_2O_4 using DFT method considering the spin-orbit interaction.

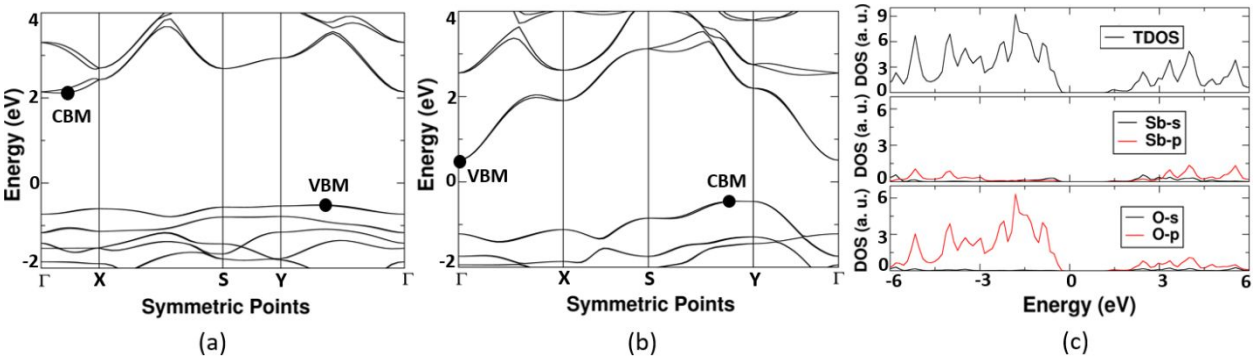

Figure 4: (a, b) DFT band structures of γ-Sb_2O_4, and δ-Sb_2O_4 monolayers (c) density of states of bulk γ-Sb_2O_4. Spin-orbit interaction is considered into account.

As DFT is known to underestimate the band gap, we perform the hybrid DFT (HSE) calculation (including spin-orbit interaction) to better approximate the gap values.[41–43] We find the corresponding band gaps as 2.99 and 3.85 eV for the bulk and monolayer γ-Sb_2O_4, 2.05 and 1.56 eV for the bulk and monolayer δ-Sb_2O_4, respectively. To further improve the prediction of the band gaps of these phases, we employ the GW method[44–46] on top of DFT to include the quasiparticles effect. As the convergence under the GW method requires a sufficiently large number of empty conduction bands, we include 60 (17 of them are occupied) bands in our calculations, making sure that the supplied empty bands are sufficient for accurate results. From the GW approximation, the QP effect increases the band gaps to 3.66 eV, 5.55 eV, 2.25 eV, and 3.39 eV for bulk γ-Sb_2O_4,

monolayer γ-Sb_2O_4, bulk δ-Sb_2O_4, and monolayer δ-Sb_2O_4, respectively (see Table 2). The large band gap values, especially in γ- and δ-Sb_2O_4 monolayers, are beneficial for their potential applications as a ferroelectric material in electronic devices. We note that in the actual devices, the substrate will play important roles. A computational study of the substrate effects on SnTe[47] shows that ferroelectricity can be either enhanced or disrupted depending on the choice of substrate. Furthermore, ionic impurities and electric charge can accumulate at the interfaces between 2D materials and the substrates in actual devices, which may degrade the ferroelectric properties. The substrate electric polarization and its impact can be estimated by carrying out DFT calculations in heterostructure models containing both 2D Sb_2O_4 and the substrate, similar to those done in SnTe.[47]

Table 2: Band gaps of γ-Sb_2O_4, and δ-Sb_2O_4 phases under different methods

Phase	DFT Band gap (eV)	HSE Band gap (eV)	GW Band gap (eV)
γ-Sb_2O_4 (bulk)	1.84	2.99	3.66
γ-Sb_2O_4 (monolayer)	2.63	3.85	5.51
δ-Sb_2O_4 (bulk)	0.63	1.56	2.25
δ-Sb_2O_4 (monolayer)	0.96	2.05	3.39

Raman spectroscopy is a widely used technique to characterize materials. To facilitate the experimental exploration of the predicted Sb_2O_4 structures, we calculated the Raman spectra as shown in Figure 5 for the bulk and monolayers. In the bulk γ-Sb_2O_4 (Fig. 5(a)), two major Raman peaks are observed at 525 and 583 cm^{-1}, whereas in the monolayer (Fig. 5(b)), four peaks are observed at 444, 558, 610, and 699 cm^{-1}. Two major Raman peaks are observed at 511 and 635 cm^{-1} in bulk δ-Sb_2O_4 (Fig. 5(c)) and 378 and 526 cm^{-1} in the monolayer (Fig. 5(d)). In addition to the major peaks, some minor Raman peaks are also shown in the spectra. The detailed tabulation of the vibration modes is shown in Supplementary Information, Section IV. In addition to the Raman spectra, we also present the simulated XRD results using Cu-k alpha method in Supplementary Information, Section V to further assist experiments.

ARTICLE

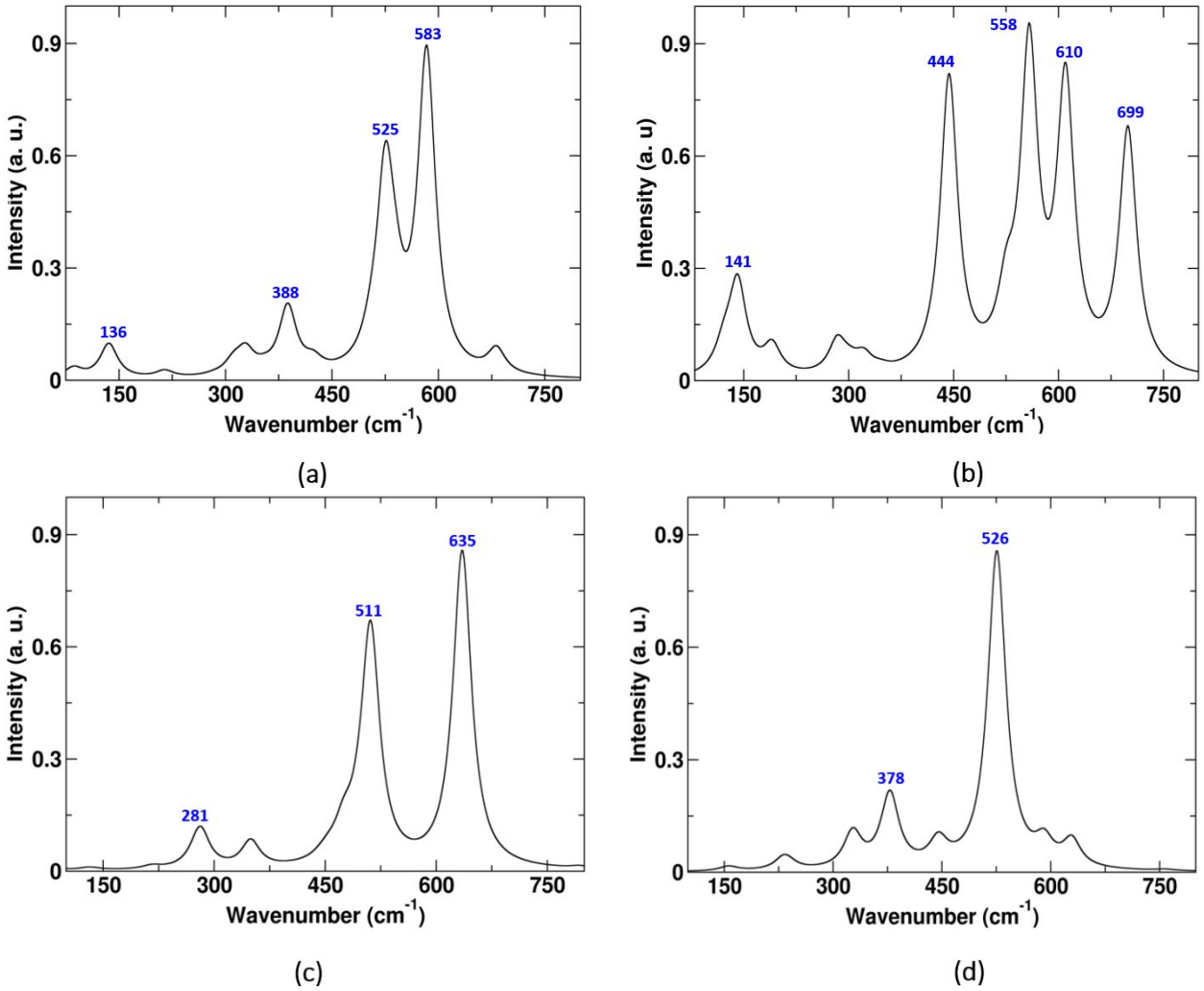

Figure 5: Calculated Raman spectra of (a) bulk γ-Sb_2O_4, (b) γ-Sb_2O_4 monolayer, (c) bulk δ-Sb_2O_4, and (d) δ-Sb_2O_4 monolayer.

Conclusions

Using the evolutionary algorithm combined with the first-principles DFT calculations, we predict the first two-dimensional (2D) polymorphs of antimony dioxide, namely, γ-Sb_2O_4 and δ-Sb_2O_4. Out-of-plane ferroelectricity is found in γ-Sb_2O_4, while in-plane ferroelectricity is found in δ-Sb_2O_4. We also show that doping with other group V elements or applying strain can lower the switching energy barriers. The dipole moment of γ-Sb_2O_4 and δ-Sb_2O_4 are calculated as 36.63 and 14.96 eÅ per unit cell, respectively, implying they

are good candidates for ferroelectric applications. Furthermore, calculations show the indirect band gaps of 5.51 and 3.39 eV for γ- and δ-Sb_2O_4 in their monolayers, respectively. Raman spectra are predicted to pave the way for the experimental investigation of the predicted structures. The existence of both in-plane and out-of-plane 2D ferroelectricity and the large band gap are notable features of these new phases, which may be of interest for potential applications.

Author Contributions

X. S. and K. N. conceived the idea of the project. R. B. performed the calculations and wrote the manuscript.

Conflicts of interest

There are no conflicts to declare.

Acknowledgements

This work at the University of Memphis was supported by the National Science Foundation under Grant No. DMR 1709528 and by the Ralph E. Powe Jr. Faculty Enhancement Awards from Oak Ridge Associated Universities (ORAU). Computational resources were provided by the High-Performance Computing Center (HPCC) at the University of Memphis. It is also partially supported by the U.S. Department of Energy, Office of Science, Office of Basic Energy Sciences Energy Frontier Research Centers program under the Award Number DESC0021118.

Notes and references

1 J. F. Scott, *Science*, 2007, **315**, 954–959.

2 N. Setter, D. Damjanovic, L. Eng, G. Fox, S. Gevorgian, S. Hong, A. Kingon, H. Kohlstedt, N. Y. Park, G. B. Stephenson, I. Stolitchnov, A. K. Taganstev, D. V. Taylor, T. Yamada and S. Streiffer, *J. Appl. Phys.*, 2006, **100**, 051606.

3 W. Zhong, R. D. King-Smith and D. Vanderbilt, *Phys. Rev. Lett.*, 1994, **72**, 3618–3621.

4 I. P. Batra, P. Wurfel and B. D. Silverman, *Phys. Rev. Lett.*, 1973, **30**, 384–387.

5 P. Sharma, F.-X. Xiang, D.-F. Shao, D. Zhang, E. Y. Tsymbal, A. R. Hamilton and J. Seidel, *Sci. Adv.*, 2019, **5**, eaax5080.

6 Y. Zhou, D. Wu, Y. Zhu, Y. Cho, Q. He, X. Yang, K. Herrera, Z. Chu, Y. Han, M. C. Downer, H. Peng and K. Lai, *Nano Lett.*, 2017, **17**, 5508–5513.

7 K. Chang, J. Liu, H. Lin, N. Wang, K. Zhao, A. Zhang, F. Jin, Y. Zhong, X. Hu, W. Duan, Q. Zhang, L. Fu, Q.-K. Xue, X. Chen and S.-H. Ji, *Science*, 2016, **353**, 274–278.

8 F. Liu, L. You, K. L. Seyler, X. Li, P. Yu, J. Lin, X. Wang, J. Zhou, H. Wang, H. He, S. T. Pantelides, W. Zhou, P. Sharma, X. Xu, P. M. Ajayan, J. Wang and Z. Liu, *Nat. Commun.*, 2016, **7**, 12357.

9 Z. Fei, W. Zhao, T. A. Palomaki, B. Sun, M. K. Miller, Z. Zhao, J. Yan, X. Xu and D. H. Cobden, *Nature*, 2018, **560**, 336–339.

10 J. Xiao, H. Zhu, Y. Wang, W. Feng, Y. Hu, A. Dasgupta, Y. Han, Y. Wang, D. A. Muller, L. W. Martin, P. Hu and X. Zhang, *Phys. Rev. Lett.*, 2018, **120**, 227601.

11 Y. Gao, M. Wu and X. Cheng Zeng, *Nanoscale Horiz.*, 2019, **4**, 1106–1112.

12 M. Wu and X. C. Zeng, *Nano Lett.*, 2016, **16**, 3236–3241.

13 W. Ding, J. Zhu, Z. Wang, Y. Gao, D. Xiao, Y. Gu, Z. Zhang and W. Zhu, *Nat. Commun.*, 2017, **8**, 14956.

14 W. Gao and J. R. Chelikowsky, *Nano Lett.*, 2020, **20**, 8346–8352.

15 N. Higashitarumizu, H. Kawamoto, C.-J. Lee, B.-H. Lin, F.-H. Chu, I. Yonemori, T. Nishimura, K. Wakabayashi, W.-H. Chang and K. Nagashio, *Nat. Commun.*, 2020, **11**, 2428.

16 K. Chang, F. Küster, B. J. Miller, J.-R. Ji, J.-L. Zhang, P. Sessi, S. Barraza-Lopez and S. S. P. Parkin, *Nano Lett.*, 2020, **20**, 6590–6597.

17 S. Wolff, R. Gillen, M. Assebban, G. Abellán and J. Maultzsch, *Phys. Rev. Lett.*, 2020, **124**, 126101.

18 K. A. Messalea, N. Syed, A. Zavabeti, M. Mohiuddin, A. Jannat, P. Aukarasereenont, C. K. Nguyen, M. X. Low, S. Walia, B. Haas, C. T. Koch, N. Mahmood, K. Khoshmanesh, K. Kalantar-Zadeh and T. Daeneke, *ACS Nano*, 2021, **15**, 16067–16075.

19 K. Yang, T. Zhang, B. Wei, Y. Bai, S. Jia, G. Cao, R. Jiang, C. Zhang, E. Gao, X. Chang, J. Li, S. Li, D. Zhu, R. Tai, H. Zhou, J. Wang, M. Zeng, Z. Wang and L. Fu, *Nat. Commun.*, 2020, **11**, 2502.

20 C. A. Cody, L. DiCarlo and R. K. Darlington, *Inorg. Chem.*, 1979, **18**, 1572–1576.

21 E. J. Roberts and F. Fenwick, *J. Am. Chem. Soc.*, 1928, **50**, 2125–2147.

22 A. C. Skapski and D. Rogers, *Chem. Commun. Lond.*, 1965, 611–613.

23 D. J. Stewart, O. Knop, C. Ayasse and F. W. D. Woodhams, *Can. J. Chem.*, 1972, **50**, 690–700.

24 J. P. Allen, J. J. Carey, A. Walsh, D. O. Scanlon and G. W. Watson, *J. Phys. Chem. C*, 2013, **117**, 14759–14769.

25 J. Nilsson, A. Landa-Cánovas, S. Hansen and A. Andersson, *Catal. Today*, 1997, **33**, 97–108.

26 H. Matsumura, K. Okumura, T. Shimamura, N. Ikenaga, T. Miyake and T. Suzuki, *J. Mol. Catal. Chem.*, 2006, **250**, 122–130.

27 J. H. Youk, A. Boulares, R. P. Kambour and W. J. MacKnight, *Macromolecules*, 2000, **33**, 3600–3605.

28 H. Galïp, H. Hasïpoğlu and G. Gündüz, *J. Appl. Polym. Sci.*, 1999, **74**, 2906–2910.

29 E. D. Weil, S. Levchik and P. Moy, *J. Fire Sci.*, 2006, **24**, 211–236.

30 M. Brebu, E. Jakab and Y. Sakata, *J. Anal. Appl. Pyrolysis*, 2007, **79**, 346–352.

31 S. Zhang, W. Zhou, Y. Ma, J. Ji, B. Cai, S. A. Yang, Z. Zhu, Z. Chen and H. Zeng, *Nano Lett.*, 2017, **17**, 3434–3440.

32 D. Amoroso and S. Picozzi, *Phys. Rev. B*, 2016, **93**, 214106.

33 E. Fatuzzo, G. Harbeke, W. J. Merz, R. Nitsche, H. Roetschi and W. Ruppel, *Phys. Rev.*, 1962, **127**, 2036–2037.

34 W. Wang, S. Dai, X. Li, J. Yang, D. J. Srolovitz and Q. Zheng, *Nat. Commun.*, 2015, **6**, 7853.

35 B. Rasche, J. Brunner, T. Schramm, M. P. Ghimire, U. Nitzsche, B. Büchner, R. Giraud, M. Richter and J. Dufouleur, *Nano Lett.*, 2022, **22**, 3550–3556.

36 X. Tang, J. Shang, Y. Gu, A. Du and L. Kou, *J. Mater. Chem. A*, 2020, **8**, 7331–7338.

37 M. Noor-A-Alam, O. Z. Olszewski and M. Nolan, *ACS Appl. Mater. Interfaces*, 2019, **11**, 20482–20490.

38 S. Song, H. M. Jang, N.-S. Lee, J. Y. Son, R. Gupta, A. Garg, J. Ratanapreechachai and J. F. Scott, *NPG Asia Mater.*, 2016, **8**, e242–e242.

39 D. D. Sante, A. Stroppa and S. Picozzi, *Phys. Chem. Chem. Phys.*, 2012, **14**, 14673–14681.

40 A. Audzijonis, J. Grigas, A. Kajokas, S. Kvedaravičius and V. Paulikas, *Ferroelectrics*, 1998, **219**, 37–45.

41 J. Heyd and G. E. Scuseria, *J. Chem. Phys.*, 2004, **121**, 1187–1192.

42 J. Heyd, G. E. Scuseria and M. Ernzerhof, *J. Chem. Phys.*, 2006, **124**, 219906.

43 J. Heyd, G. E. Scuseria and M. Ernzerhof, *J. Chem. Phys.*, 2003, **118**, 8207–8215.

44 L. Hedin, *Phys. Rev.*, 1965, **139**, A796–A823.

45 M. S. Hybertsen and S. G. Louie, 24.

46 G. Onida, L. Reining and A. Rubio, *Rev. Mod. Phys.*, 2002, **74**, 601–659.

47 Z. Fu, M. Liu and Z. Yang, *Phys. Rev. B*, 2019, **99**, 205425.